communications physics

Article

https://doi.org/10.1038/s42005-025-01959-9

Feedback-induced nonlinear spin dynamics in an inhomogeneous magnetic field

Check for updates

Tishuo Wang[1,2], Zhihuang Luo[1,2] ✉, Shizhong Zhang[3] & Zhenhua Yu[1,2] ✉

Nonlinear spin dynamics is essential for predicting complex behaviors of spin systems and has a wide range of applications in physics. Although spin systems have been extensively studied, many intricate behaviors such as self-organizing or chaotic oscillations still need to be better understood with a thorough analysis of nonlinear dynamics. Here we investigate the coupled dynamics of a collection of spins with multiple Larmor frequencies for modeling an inhomogeneous magnetic field and reveal that the nonlinearity induced by a feedback scheme leads to much richer stable dynamic phases, including quasi-periodic orbits and chaos besides the usual limit cycles. We further discuss the robustness of these dynamical phases against experimental noises and the feasibility of realization in various spin systems. Our findings contribute to future observation of nonlinear dynamical phases and prospective applications in spin masers, time crystals and quasi-crystals, and precision measurement.

Nonlinear systems that exhibit self-organizing oscillations or chaotic dynamical behavior are of great interest to physicists[1–3]. For example, lasers (masers) are nonlinear systems that, when external pumping strength exceeds a certain threshold, begin to oscillate in phase and emit coherent lights (microwaves)[4–11], providing frequency references crucial for precision measurement. To extend to low-frequency domains and operate continuously under ambient conditions without cryogenic refrigeration and high-vacuum cavities, spin maser technologies were developed to replace cavities with feedback coils[12–14]; the nonlinearity brought about by the feedback magnetic field generated by the coils can sustain the precession of atomic spins around an external bias magnetic field at the Larmor frequency, which corresponds to a dynamical phase of limit cycles. The spin maser properties of noble gases have been extensively studied[15–18] due to their long nuclear spin coherent times protected by the closed-shell electronic configurations and high degrees of population inversion achieved via the spin-exchange collisions with auxiliary alkali-metal atoms which can be optically pumped[19].

Self-organizing oscillations in spin masers can persist far beyond the transverse relaxation time T_2, permitting long-time coherent measurement of frequencies with greater precision[16,20]. Employment of multiple species of atoms can further mitigate uncertainty arising from long-term drifts of bias magnetic field[21–25]. These features are extremely advantageous for precision measurements, such as in search of permanent electric dipole moments (EDMs)[20,26], tests of Lorentz and CPT violation[27,28], and probes of dark matter[29,30]. All such new physics, if ever existent, is conceived to bring about corrections, though maybe extremely small, to eigen-energies of subject quantum systems, whose clue can be looked for in spectroscopies[28]; precise measurement of frequencies in spin masers may reveal such corrections. For example, experiments to search EDMs are designed to measure the difference in the precession frequency of spins under a bias magnetic field when exposed to different electric field configurations[26,31]. However, in situations when spin masers utilize multiple species of atoms, in which multiple intrinsic Larmor frequencies exist as the gyromagnetic ratios of different species are different, previous works usually treat the oscillation of each species independently[24]. Such an approximation, though rendering agreements with experiments in certain limited situations, hardly constitutes a complete picture of the nonlinear spin dynamics in the presence of multiple intrinsic Larmor frequencies[32].

In this work, we study the nonlinear dynamics of a collection of spins subjected to a common feedback magnetic field and a static inhomogeneous magnetic field. The inhomogeneity of the field results in different Larmor frequencies acting on spins. We first consider a situation with binary Larmor frequencies and find that the nonlinear spin dynamics are much richer than that for a single-bias magnetic field. The resulting phase diagram consists of not only stable limit cycles that appear in previous works but also quasi-periodic orbits and chaos. In the phase of limit cycles, all the spins, regardless of their intrinsic Larmor frequencies, manage to synchronize and sustain a sinusoidal oscillation at the central frequency. In the phase of quasi-periodic

[1]Guangdong Provincial Key Laboratory of Quantum Metrology and Sensing & School of Physics and Astronomy, Sun Yat-Sen University (Zhuhai Campus), 519082 Zhuhai, China. [2]State Key Laboratory of Optoelectronic Materials and Technologies, Sun Yat-Sen University (Guangzhou Campus), 510275 Guangzhou, China. [3]Department of Physics and Hong Kong Institute of Quantum Science and Technology, The University of Hong Kong, Hong Kong, China.
✉e-mail: luozhih5@mail.sysu.edu.cn; huazhenyu2000@gmail.com

orbits, the Fourier transform of the transverse spin component peaks at multiple frequencies with equal spacing. Both limit cycles and quasi-periodic orbits exhibit robust self-organizing patterns in time and ultra-high resolution spectra in frequency. In the phase of chaos, the dynamics are found to have a close resemblance to the butterfly pattern of the well-known Lorenz equations[33].

The limit cycles and the quasi-periodic orbits established here can be considered as a realization of the phases of time crystals and time quasi-crystals; the former is a phase of matter breaking continuous time-translational symmetry, whose observables oscillate in time with a single fixed period[34,35], while the latter, an extension to the former, exhibits quasi-periodic oscillations in time[36,37]. We show that it is possible to tune between the limit cycles and the quasi-periodic orbits by changing parameters, which provides an opportunity to study the transition between the time crystal and time quasi-crystal phases[34–40].

We then discuss the generalization to more than two intrinsic Larmor frequencies and even the continuum case. We argue that limit cycles, quasi-periodic orbits, and chaos are the general phases of the nonlinear spin dynamics in the presence of multiple intrinsic Larmor frequencies. Thus dynamics in such a general class of systems provides a wide range of potential applications in multimode spin masers, time crystals and quasi-crystals, and precision measurement. Finally, we point out the possibility of experimental realization in spin systems such as alkali-metal atoms, noble gases, and liquid nuclear magnetic resonance.

Results

Formalism

We consider a collection of N spins in an inhomogeneous bias magnetic field along the $\hat{z}$-direction and a feedback field along $\hat{x}$- and $\hat{y}$-directions, i.e., $\mathbf{B} = (B_x^{\rm fb}, B_y^{\rm fb}, B_0^j)$, where B_0^j is assumed to be a local bias field experienced by the jth spin for simulating the inhomogeneous magnetic field. Therefore, the dynamics of spin polarization vector $\mathbf{P}_j = (P_{j,x}, P_{j,y}, P_{j,z})$ can be described by a set of nonlinear Bloch equations

$$\frac{\mathrm{d}P_{j,x}}{\mathrm{d}t} = \omega_j P_{j,y} - \gamma B_y^{\rm fb} P_{j,z} - \frac{P_{j,x}}{T_2}, \tag{1}$$

$$\frac{\mathrm{d}P_{j,y}}{\mathrm{d}t} = -\omega_j P_{j,x} + \gamma B_x^{\rm fb} P_{j,z} - \frac{P_{j,y}}{T_2}, \tag{2}$$

$$\frac{\mathrm{d}P_{j,z}}{\mathrm{d}t} = \gamma B_y^{\rm fb} P_{j,x} - \gamma B_x^{\rm fb} P_{j,y} - \frac{P_{j,z} - P_0}{T_1}. \tag{3}$$

Here, P_0 denotes the equilibrium polarization (due to pumping), γ is the gyromagnetic ratio of spin, T_1 and T_2 stand for the (effective) spin longitudinal and transverse relaxation times. The Larmor frequency $\omega_j = \gamma B_0^j$ for the jth spin can be different due to the inhomogeneity of the bias field. All spins are subjected to a common feedback field: $B_x^{\rm fb}(t) = \frac{\alpha}{\gamma}\overline{P}_y(t)$ and $B_y^{\rm fb}(t) = -\frac{\alpha}{\gamma}\overline{P}_x(t)$ that are proportional to the transverse components of the average spin polarization defined as $\overline{\mathbf{P}}(t) \equiv (1/N)\sum_{j=1}^{N}\mathbf{P}_j(t)$. This feedback field can be realized by feeding the measured signals of $\overline{P}_x(t)$ and $\overline{P}_y(t)$ back into pairs of Helmholtz coils with the feedback gain $\alpha(>0)$[16]. In the case when the bias magnetic field is homogeneous, i.e., ω_j are identical, it has been shown that the no signal fixed point $\mathbf{P}_j = \mathbf{P}_{\rm NS} \equiv (0, 0, P_0)$, corresponding to zero transverse spin polarization, becomes unstable once α exceeds the critical value $\alpha_c \equiv 1/T_2P_0$. For $\alpha > \alpha_c$, a new stable limit cycle solution emerges for which non-zero transverse spin polarization processes at the identical Larmor frequency, corresponding to the onset of maser[16].

Binary Larmor frequencies

To investigate the effects of an inhomogeneous bias magnetic field, we start by considering the situation of binary Larmor frequencies in which half of the spins are subject to $\omega_1 = \omega_c + \epsilon/2$ and the other half $\omega_2 = \omega_c - \epsilon/2$. Without loss of generality, we assume $\epsilon > 0$. In this case, we only need to consider two representative spins $\mathbf{P}_1$ and $\mathbf{P}_2$, equivalent to taking $N = 2$ in Eqs. (1)–(3). The coupled Bloch equations in this binary case are six-dimensional; trajectories of the long-time stable solutions obtained by numerically solving the equations would be rather difficult to analyze and visualize. In experiments, however, the spins are usually prepared in the same initial state, i.e., $\mathbf{P}_1(t=0) = \mathbf{P}_2(t=0)$. Starting from this initial condition, we can prove that subsequent evolution maintains $P_{1,z} = P_{2,z}$ and $|P_{1,T}| = |P_{2,T}|$ at any time t with $P_{j,T} \equiv P_{j,x} + iP_{j,y}$ the complex transverse component (details in Supplementary Note 1). These two features allow us to reduce the dimension of the nonlinear system. The second feature ensures that the mean component $\overline{P}_T \equiv (P_{1,T} + P_{2,T})/2$ is perpendicular to the difference $\Delta P_T \equiv P_{1,T} - P_{2,T}$, which prompts us to parameterize $\overline{P}_T = Ae^{i\theta}/2$ and $\Delta P_T = Be^{i(\theta+\pi/2)}$ with real amplitudes A and B and phase angle θ. Consequently, the Bloch equations are reduced to the form

$$\frac{\mathrm{d}A}{\mathrm{d}t} = \alpha\overline{P}_z A + \epsilon B/2 - A/T_2, \tag{4}$$

$$\frac{\mathrm{d}B}{\mathrm{d}t} = -\epsilon A/2 - B/T_2, \tag{5}$$

$$\frac{\mathrm{d}\overline{P}_z}{\mathrm{d}t} = -\alpha A^2/4 - (\overline{P}_z - P_0)/T_1, \tag{6}$$

$$\frac{\mathrm{d}\theta}{\mathrm{d}t} = -\omega_c. \tag{7}$$

Since the phase angle can be readily solved as $\theta(t) = -\omega_c t + \phi$ with ϕ an arbitrary phase, the remaining dynamical system is reduced to three dimensions regarding $\{A, B, \overline{P}_z\}$. In the following, we will use dimension reduction to simplify our analysis. For initial conditions, other than $\mathbf{P}_1(t=0) = \mathbf{P}_2(t=0)$, see discussions in Supplementary Note 1 for details.

Stable phase diagram

Figure 1 represents the stable dynamical phases of binary Larmor frequencies. When α is sufficiently large, the system is found to exhibit rich phases: limit cycles for relatively small ϵ, quasi-periodic orbits for relatively large ϵ, and chaos in between. The boundaries of the stable dynamical phases marked by the solid lines in Fig. 1 are obtained analytically via the linear stability analysis (details in Supplementary Note 2), whereas those marked by discrete symbols are determined numerically by taking the parameters $P_0 = 0.0174833$, $1/T_1 = 0.11348$ Hz, $1/T_2 = 0.148$ Hz, and $\omega_c/2\pi = 8.85$ Hz from ref. 41, whose experimental system is an atomic magnetometer utilizing the nuclear spins of a ^{129}Xe gas pumped by auxiliary Rb atoms via spin-exchange collision (details in Supplementary Note 3).

(a) Limit cycles. In a dynamical system, a closed trajectory in the phase space constitutes a limit cycle solution if there exists at least another trajectory spiraling into it either as time $t \to \infty$ or as time $t \to -\infty$; the former is called stable as the latter unstable[1]. The stable limit cycle solution is also called the masing phase. When $\epsilon = 0$, our system reduces to the previously studied one-species spin masers[16,20]. Figure 1 shows that the stable limit cycle phase extends into the region where $\epsilon \neq 0$. However, to escape from the trivial phase, one needs $\alpha/\alpha_c > f(\epsilon T_2)$ with $f(x) \equiv 1 + (x/2)^2$; the larger ϵ is, the larger the threshold value of the gain α is required. The limit cycle solution can be derived by setting the left-hand sides of Eqs. (4)–(6) to zero. We find a pair of nontrivial twin fixed points: $A_{\rm LC,\pm} = \pm 2\{P_0[\alpha - \alpha_c f(\epsilon T_2)]/T_1\}^{1/2}/\alpha$, $B_{\rm LC,\pm} = -\epsilon T_2 A_{\rm LC,\pm}/2$ and $\overline{P}_{z,\rm LC} = f(\epsilon T_2)/\alpha T_2$, which are equivalent to the limit cycle solution of Eqs. (1)–(3), i.e., $P_{j,T} = [1 + i(-1)^j \epsilon T_2/2]\overline{P}_T$, $P_{1,z} = P_{2,z} = \overline{P}_{z,\rm LC}$ with $\overline{P}_T = e^{-i(\omega_c t - \phi)}|A_{\rm LC,\pm}|/2$; the pair of the twin fixed points correspond to two periodic orbits of the limit cycles whose phase angles ϕ differ by π.

The limit cycle phase is stable in the region left to the line $\alpha/\alpha_c = 3y/2 + (1 - T_2/T_1)/2(y - T_2/T_1)$ for $\min(1, T_2/T_1) < y < \max(1, T_2/T_1)$ with $y \equiv$

$(\epsilon T_2/2)^2$ (see also Supplementary Note 2). The line starts at the point $\epsilon = 2/T_2$ and $\alpha = 2\alpha_c$ and approaches the asymptote $\epsilon = 2/\sqrt{T_1 T_2}$ as $\alpha \to \infty$. Across the line, a Hopf bifurcation occurs, rendering the limit cycles unstable (see also Supplementary Note 2). The stable dynamical behaviors of limit cycles are given in Fig. 2a–d. The sinusoidal oscillation of $\overline{P}_T(t)$ gives rise to a signal at the masing frequency $\omega_s = \omega_c$, and the natural linewidth ($\propto 1/T_2$) disappears in the feedback scheme. It is very important to suppress the uncertainty of the masing frequency and achieve higher precision in measurement[30].

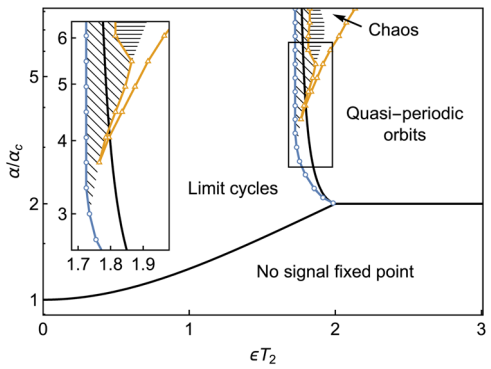


Fig. 1 | Stable phase diagram. This diagram illustrates the stable regions of limit cycles, quasi-periodic orbits, chaos, and the no signal fixed point, depending on the feedback gain α and the difference ϵ of binary Larmor frequencies. The boundaries, represented by the three black lines, are defined as follows: (i) $\alpha/\alpha_c = 1 + (\epsilon T_2/2)^2$ for $\epsilon T_2 < 2$, (ii) $\alpha/\alpha_c = 2$ for $\epsilon T_2 \geq 2$, and (iii) $\alpha/\alpha_c = 3y/2 + (1 - T_2/T_1)/2(y - T_2/T_1)$ for $\min(1, T_2/T_1) < y < \max(1, T_2/T_1)$, where $y \equiv (\epsilon T_2/2)^2$. The triangle and circle symbols mark the boundaries of stable regions as determined numerically, with the blue and orange lines connecting the symbols serving as guides for the eye. Notably, overlaps exist among stable regions. The features $P_{1,z} = P_{2,z}$ and $|P_{1,T}| = |P_{2,T}|$ are maintained by the stable trajectories obtained numerically, except in the diagonally slashed area for the quasi-periodic orbits and the horizontally slashed area for the chaos. The inset shows a zoom-in of the boxed part.

(b) Quasi-periodic orbits. In contrast, to limit cycles, a quasi-periodic motion of a dynamical system consists of two or more incommensurable frequencies such that the corresponding trajectory is not closed[1]. In the region of $\alpha > 2\alpha_c$ for $\epsilon T_2 > 2$, the stable solution of our system turns out to be quasi-periodic orbits. This can be understood in the large ϵ limit. Since ϵ is much larger than any other energy scale, to the lowest order, $\mathbf{P}_1$ and $\mathbf{P}_2$ precess with frequencies ω_1 and ω_2, respectively. The previous treatment approximating spin oscillations of different species independently corresponds to this limit[24]. Note that given two randomly chosen *real* values for ω_1 and ω_2 respectively, in principle, the probability of the ratio ω_1/ω_2 being rational is negligible compared with that of being irrational. In practice, with the values of the two frequencies rounded to certain decimal digits, however, the commensurate period would usually be rather long ($\gg 1/\omega_1, 1/\omega_2$) such that within experimental duration (usually smaller than the commensurate period), $\overline{\mathbf{P}}(t)$ shall generally be essentially quasi-periodic. Going beyond the lowest order does not change the nature of quasi-periodic orbits.

In the phase of quasi-periodic orbits, the trajectories of $\overline{\mathbf{P}}(t)$ look rather dense as shown in Fig. 2e. However, once represented in terms of $\{A, B, \overline{P}_z\}$, the quasi-periodic orbits unify into a limit cycle solution as shown in Fig. 2f. Note that this limit cycle solution generally has a three-dimensional configuration, and its period τ, while independent of ω_c, changes with α and ϵ (more details in Supplementary Note 4). Given Eqs. (4)–(6) are invariant under the transform $\{A, B, \overline{P}_z\}$ to $\{-A, -B, \overline{P}_z\}$, the absolute value of the Fourier transform amplitude of $\overline{P}_x(t)$ or $\overline{P}_y(t)$ peaks at regular frequencies $\omega_c + 2\pi(2n+1)/\tau$ with integer n as shown in Fig. 2h. The quasi-periodic orbit phase found in our spin system provides a realization for multi-mode

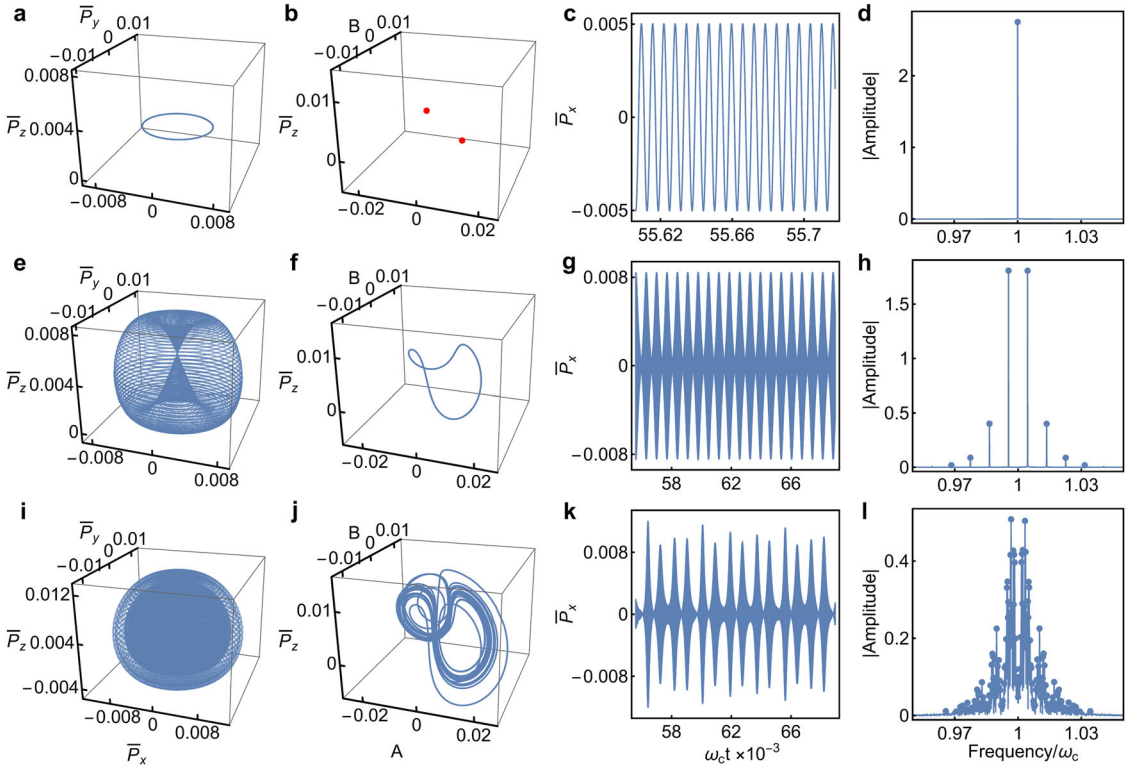


Fig. 2 | Stable dynamical behaviors. a–d The trajectory of the overall mean polarization $\overline{\mathbf{P}}(t)$, the corresponding trajectory in the phase space of $\{A, B, \overline{P}_z\}$, the time series of $\overline{P}_x(t)$, and the absolute value of the Fourier transform amplitude of $\overline{P}_x(t)$ in arbitrary units for limit cycles, respectively. **e–h** Present the same aspects for quasi-periodic orbits. **i–l** Display the corresponding behaviors for chaos. In the phase space of $\{A, B, \overline{P}_z\}$, the limit cycles condense into twin fixed points $(A_{\mathrm{LC},\pm}, B_{\mathrm{LC},\pm}, \overline{P}_{z,\mathrm{LC}})$, the quasi-periodic orbits unify into a limit cycle solution, and the chaotic trajectories resemble the well-known Lorenz equations. The parameters used are $\alpha/\alpha_c = 7.8$ and $\epsilon T_2 = 1$, 3, and 2 for **a–d**, **e–h**, and **i–l**, respectively.

excitations. Such multi-mode excitations are useful to eliminate uncorrelated noise in the frequency domain[42].

(c) Chaos. High sensitivity to initial conditions is a hallmark of chaotic dynamic motions[1,43,44]. Interacting magnetic systems can generally exhibit chaotic motions under appropriate conditions[2,3]. In our system, effective interaction is introduced by the feedback field $B_x^{\rm fb}(t)$ and $B_y^{\rm fb}(t)$. In Fig. 1, we locate the stable region of the chaos phase largely in between the limit cycle phase and the quasi-periodic orbit phase. The exact locations of the chaos phase depend sensitively on the parameters of the system[1]. In contrast to Fig. 2i, when the chaotic trajectories are presented in terms of $\{A, B, \overline{P}_z\}$ as in Fig. 2j, a butterfly pattern reminiscent of the well-known Lorenz equations emerges. Figure 2l shows that the Fourier transform of the transverse amplitude in the chaotic regime peaks irregularly. An alternative quantitative way to distinguish chaos from other stable orbits, e.g, quasi-periodic orbits, is via the Lyapunov exponents, which essentially quantify the rates of how fast deviations in initial conditions can grow; the largest Lyapunov exponent is positive for the former and zero for the latter. The exponent can be either numerically calculated from a known dynamic system[43,44], or estimated from a time series of data collected in experiment[45] (see also Supplementary Note 5).

Robustness

Due to the nonlinear nature of our dynamical system, the predicted limit cycle, quasi-periodic orbit, and chaotic phases are robust against experimental perturbations. For instance, to evaluate the effects of fluctuations from the feedback mechanism, we consider two fluctuating fields, $f_\sigma(t)$ and $g_\sigma(t)$, appearing in the feedback fields as $B_x^{\rm fb} = [\alpha\overline{P}_y + f_\sigma(t)]/\gamma$ and $B_y^{\rm fb} = [-\alpha\overline{P}_x + g_\sigma(t)]/\gamma$. At any time t, $f_\sigma(t)$ and $g_\sigma(t)$ sample randomly from the range $[-\sigma, \sigma]$. Under the influence of the fluctuations with strength σ, the time series of stable dynamics denoted by $q_\sigma(t)$ can be different from $q_0(t)$ for $\sigma = 0$. To quantify the robustness of the dynamical phase corresponding to $q_0(t)$, we define the function (see also Supplementary Note 8).

$$\mathcal{R} = \frac{\int |\tilde{q}_0(\omega)\tilde{q}_\sigma(\omega)|\mathrm{d}\omega/2\pi}{\sqrt{\int |\tilde{q}_0(\omega)|^2\mathrm{d}\omega/2\pi \int |\tilde{q}_\sigma(\omega')|^2\mathrm{d}\omega'/2\pi}}. \quad (8)$$

where $\tilde{q}_\sigma(\omega)$ is the Fourier transform of $q_\sigma(t)$. Figure 3a and c show the robustness of the limit cycles and quasi-periodic orbits calculated from the time series of $\overline{P}_x(t)$ with and without the fluctuations of the feedback field. We can see that the cut-off noise strength $\sigma_{\rm cut} \approx 3$ and ≈ 1.5 for the limit cycle and the quasi-periodic orbit respectively, at which $\mathcal{R}$ decreases to $1/e$; single-shot spectra of $\overline{P}_x(t)$ representative across the cut-off are shown in Fig. 3b and d. Figure 3 shows that the limit cycles of a single peak in the frequency domain seem more robust than the quasi-periodic orbits, which may be due to the fact that the latter are subject to the noise at their *multiple* peaks simultaneously. Other practical matters relevant to the experiment, such as glitches in setups and fluctuations and drifts in the bias field, are also considered in Supplementary Note 8.

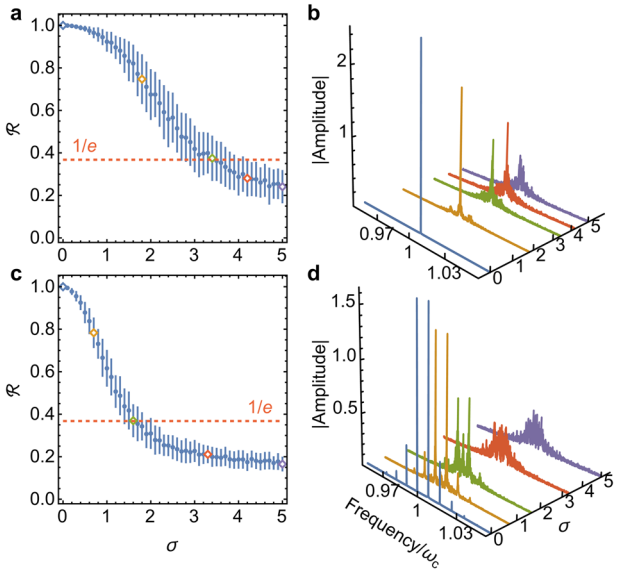


Fig. 3 | Robustness against the fluctuations of the feedback field. a Shows the function $\mathcal{R}$ for limit cycles as a function of fluctuation strength σ. Each data point represents the average of 100 individual simulations, with error bars indicating the standard deviations. A cut-off is set where $\mathcal{R}$ reduces to $1/e$. **b** presents the absolute amplitudes of single-shot spectra of $\overline{P}_x(t)$ for color-marked data points in (**a**). **c** illustrates the function $\mathcal{R}$ for quasi-periodic orbits as a function of σ. **d** provides the absolute amplitudes of single-shot spectra of $\overline{P}_x(t)$ for color-marked data points in (**c**). The parameters used are $\alpha/\alpha_c = 7.8, \epsilon T_2 = 1$ for **a** and **b**, and $\alpha/\alpha_c = 7.8, \epsilon T_2 = 3$ for (**c**) and (**d**).

Conclusions

In summary, we have studied the nonlinear spin dynamics with binary Larmor frequencies, and analyzed in detail its rich dynamical phases induced by a feedback scheme. As the difference of binary Larmor frequencies increases, the stable solution of the limit cycles persists until it is replaced by quasi-periodic orbits and chaotic dynamics. Due to the nonlinearity of the system, the self-sustained oscillations generated by the limit cycles and the quasi-periodic orbits are independent of the initial conditions and exhibit impressive robustness against experimental perturbations (see also Supplementary Note 8). These nonlinear oscillations are expected to sustain for arbitrary lengths of time, which are appropriate for the long-term measurement of frequency shifts such as the search for EDMs[20,28], the advances of single-mode and multimode spin masers, and can be further considered as realizations of time crystals and quasi-crystals[34–40]. It is worth emphasizing that the limit cycles demonstrate better robustness (see Fig. 3), and thus provide better precision in the presence of perturbations, while the multiple high-resolution peaks characteristic of quasi-periodic orbits can be used to rule out false signals due to local noise contaminations in the frequency domain since any true signal shall modify the multiple peaks simultaneously in a correlated way.

Our formalism can be further generalized to the cases with more than two intrinsic Larmor frequencies or in a continuum limit where the inhomogeneous Larmor frequencies follow a distribution $\rho(\omega)$ (more details in Supplementary Note 6). We find that limit cycles, quasi-periodic orbits, and chaos continue to be the generic phases of the dynamics of the coupled spins, even when the feedback magnetic field is applied only in one direction[17] (see also Supplementary Note 7). Our findings can be demonstrated experimentally in spin systems such as alkali-metal atoms, noble gases, and liquid nuclear magnetic resonance. (A proposal for the realization in spin systems can be seen in Supplementary Note 9.) We can employ a species of atomic spins (e.g., K, Rb, Cs) or nuclear spins (e.g., ^{3}He, ^{21}Ne, ^{129}Xe) applied in an inhomogeneous magnetic field (see also Supplementary Note 6) or multiple species of spins co-located in a bias field. Co-located spin masers consisting of two species of atoms, for example, ^{129}Xe and ^{131}Xe, are employed to mitigate the frequency instability due to the magnetic field and cell temperature drifts[24]. Our study indicates that these co-located nuclear spin masers can operate in the quasi-periodic orbit regime.

Data availability

Numerical data from figures are available from the corresponding author upon reasonable request.

Code availability

Computer codes for numerical calculation are available from the corresponding author upon reasonable request.

Received: 10 October 2024; Accepted: 15 January 2025;
Published online: 25 January 2025

References

1. Strogatz, S. H. *Nonlinear Dynamics and Chaos: With Applications to Physics, Biology, Chemistry, and Engineering* (CRC Press, 2018).
2. Lin, Y.-Y., Lisitza, N., Ahn, S. & Warren, W. S. Resurrection of crushed magnetization and chaotic dynamics in solution NMR spectroscopy. *Science* **290**, 118–121 (2000).
3. Abergel, D. Chaotic solutions of the feedback driven Bloch equations. *Phy. Lett. A* **302**, 17–22 (2002).
4. Maiman, T. H. Stimulated optical radiation in ruby. *Nature* **187**, 493–494 (1960).
5. Gordon, J. P., Zeiger, H. J. & Townes, C. H. Molecular microwave oscillator and new hyperfine structure in the microwave spectrum of nh_3. *Phys. Rev.* **95**, 282–284 (1954).
6. Gordon, J. P., Zeiger, H. J. & Townes, C. H. The maser—new type of microwave amplifier, frequency standard, and spectrometer. *Phys. Rev.* **99**, 1264–1274 (1955).
7. Goldenberg, H. M., Kleppner, D. & Ramsey, N. F. Atomic hydrogen maser. *Phys. Rev. Lett.* **5**, 361–362 (1960).
8. Oxborrow, M., Breeze, J. D. & Alford, N. M. Room-temperature solid-state maser. *Nature* **488**, 353–356 (2012).
9. Kraus, H. et al. Room-temperature quantum microwave emitters based on spin defects in silicon carbide. *Nat. Phys.* **10**, 157–162 (2014).
10. Breeze, J. D., Salvadori, E., Sathian, J., Alford, N. M. & Kay, C. W. M. Continuous-wave room-temperature diamond maser. *Nature* **555**, 493–496 (2018).
11. Suefke, M., Lehmkuhl, S., Liebisch, A., Blümich, B. & Appelt, S. Para-hydrogen raser delivers sub-millihertz resolution in nuclear magnetic resonance. *Nat. Phys.* **13**, 568–572 (2017).
12. Bloom, A. L. Principles of operation of the rubidium vapor magnetometer. *Appl. Opt.* **1**, 61–68 (1962).
13. Chalupczak, W. & Josephs-Franks, P. Alkali-metal spin maser. *Phys. Rev. Lett.* **115**, 033004 (2015).
14. Bevington, P., Gartman, R. & Chalupczak, W. Object detection with an alkali-metal spin maser. *J. Appl. Phys.* **130**, 214501 (2021).
15. Robinson, H. G. & Myint, T. ^{3}He nuclear zeeman maser. *Appl. Phys. Lett.* **5**, 116–118 (1964).
16. Yoshimi, A. et al. Nuclear spin maser with an artificial feedback mechanism. *Phys. Lett. A* **304**, 13–20 (2002).
17. Jiang, M., Su, H., Wu, Z., Peng, X. & Budker, D. Floquet maser. *Sci. Adv.* **7**, eabe0719 (2021).
18. Su, H., Jiang, M. & Peng, X. Review of noble-gas spin amplification via the spin-exchange collisions. *Sci. China Inf. Sci.* **65**, 200501 (2022).
19. Walker, T. G. & Happer, W. Spin-exchange optical pumping of noble-gas nuclei. *Rev. Mod. Phys.* **69**, 629–642 (1997).
20. Inoue, T. et al. Frequency characteristics of nuclear spin oscillator with an artificial feedback toward search for xe-129 atomic electric dipole moment. *Eur. Phys. J. D* **70**, 129 (2016).
21. Chupp, T. E., Hoare, R. J., Walsworth, R. L. & Wu, B. Spin-exchange-pumped ^{3}He and ^{129}Xe zeeman masers. *Phys. Rev. Lett.* **72**, 2363–2366 (1994).
22. Stoner, R. E. et al. Demonstration of a two species noble gas maser. *Phys. Rev. Lett.* **77**, 3971–3974 (1996).
23. Bear, D. et al. Improved frequency stability of the dual-noble-gas maser. *Phys. Rev. A* **57**, 5006–5008 (1998).
24. Sato, T. et al. Development of co-located ^{129}Xe and ^{131}Xe nuclear spin masers with external feedback scheme. *Phys. Lett. A* **382**, 588–594 (2018).
25. Bevington, P., Gartman, R., Stadnik, Y. V. & Chalupczak, W. Dual-frequency cesium spin maser. *Phys. Rev. A* **102**, 032804 (2020).
26. Rosenberry, M. A. & Chupp, T. E. Atomic electric dipole moment measurement using spin exchange pumped masers of ^{129}Xe and ^{3}He. *Phys. Rev. Lett.* **86**, 22–25 (2001).
27. Bear, D., Stoner, R. E., Walsworth, R. L., Kostelecký, V. A. & Lane, C. D. Limit on Lorentz and CPT violation of the neutron using a two-species noble-gas maser. *Phys. Rev. Lett.* **85**, 5038–5041 (2000).
28. Safronova, M. S. et al. Search for new physics with atoms and molecules. *Rev. Mod. Phys.* **90**, 025008 (2018).
29. Afach, S. et al. Search for topological defect dark matter with a global network of optical magnetometers. *Nat. Phys.* **17**, 1396–1401 (2021).
30. Terrano, W. A. & Romalis, M. V. Comagnetometer probes of dark matter and new physics. *Quantum Sci. Technol.* **7**, 014001 (2021).
31. Sachdeva, N. et al. New limit on the permanent electric dipole moment of ^{129}Xe using ^{3}He comagnetometry and squid detection. *Phys. Rev. Lett.* **123**, 143003 (2019).
32. Liu, G. Trispin dynamics in an alkali-metal–noble-gas nuclear-magnetic-resonance gyroscope. *Phys. Rev. A* **99**, 033409 (2019).
33. Haken, H. Analogy between higher instabilities in fluids and lasers. *Phys. Lett. A* **53**, 77–78 (1975).
34. Kongkhambut, P. et al. Observation of a continuous time crystal. *Science* **377**, 670–673 (2022).
35. Wu, X. et al. Dissipative time crystal in a strongly interacting Rydberg gas. *Nat. Phys.* **20**, 1389–1394 (2024).
36. Autti, S., Eltsov, V. B. & Volovik, G. E. Observation of a time quasicrystal and its transition to a superfluid time crystal. *Phys. Rev. Lett.* **120**, 215301 (2018).
37. Giergiel, K., Miroszewski, A. & Sacha, K. Time crystal platform: from quasicrystal structures in time to systems with exotic interactions. *Phys. Rev. Lett.* **120**, 140401 (2018).
38. Wadenpfuhl, K. & Adams, C. S. Emergence of synchronization in a driven-dissipative hot Rydberg vapor. *Phys. Rev. Lett.* **131**, 143002 (2023).
39. Ding, D. et al. Ergodicity breaking from Rydberg clusters in a driven-dissipative many-body system. *Sci. Adv.* **10**, eadl5893 (2024).
40. Huang, Y., Li, T. & Yin, Z.-Q Symmetry-breaking dynamics of the finite-size Lipkin–Meshkov–Glick model near ground state. *Phys. Rev. A* **97**, 012115 (2018).
41. Chen, L. & Ren, Y. Rapid ^{129}Xe–Rb spin-exchange rate measurement by using an atomic magnetometer. *Appl. Opt.* **59**, 3967–3970 (2020).
42. Jiang, M. et al. Floquet spin amplification. *Phys. Rev. Lett.* **128**, 233201 (2022).
43. Parker, T. S. & Chua, L. *Practical Numerical Algorithms for Chaotic Systems* (Springer Science & Business Media, 2012).
44. Sandri, M. Numerical calculation of Lyapunov exponents. *Math. J.* **6**, 78–84 (1996).
45. Rosenstein, M. T., Collins, J. J. & De Luca, C. J. A practical method for calculating largest Lyapunov exponents from small data sets. *Physica D* **65**, 117–134 (1993).

Acknowledgements

We thank Xiaodong Li and Long Wang for their discussions on numerics. T.W. and Z.Y. are supported by the National Natural Science Foundation of China Grant Nos. 12074440 and 12474270, and Guangdong Project (Grant No. 2017GC010613). Z.L. is supported by the Guangdong Basic and Applied Basic Research Foundation (Grant No. 2024A1515011406), Fundamental Research Funds for the Central Universities, Sun-Yat-Sen University (Grant No. 23qnpy63), and Guangdong Provincial Key Laboratory (Grant No. 2019B121203005). S.Z. is supported by grants from the Research Grants Council of the Hong Kong Special Administrative Region, China (HKU 17304719, HKU C7012-21GF, and an RGC Fellowship award HKU RFS2223-7S03).

Author contributions

Z.L. and Z.Y. conceived the idea and supervised the work. T.W., Z.L., S.Z., and Z.Y. developed the theoretical framework. T.W. carried out the calculations. Z.L. and Z.Y. wrote the paper. All authors commented on the manuscript.

Competing interests

The authors declare no competing interests.

Additional information

Supplementary information The online version contains supplementary material available at https://doi.org/10.1038/s42005-025-01959-9.

Correspondence and requests for materials should be addressed to Zhihuang Luo or Zhenhua Yu.

Peer review information *Communications Physics* thanks the anonymous reviewers for their contribution to the peer review of this work. A peer review file is available.

Reprints and permissions information is available at http://www.nature.com/reprints

Publisher's note Springer Nature remains neutral with regard to jurisdictional claims in published maps and institutional affiliations.

Open Access This article is licensed under a Creative Commons Attribution-NonCommercial-NoDerivatives 4.0 International License, which permits any non-commercial use, sharing, distribution and reproduction in any medium or format, as long as you give appropriate credit to the original author(s) and the source, provide a link to the Creative Commons licence, and indicate if you modified the licensed material. You do not have permission under this licence to share adapted material derived from this article or parts of it. The images or other third party material in this article are included in the article's Creative Commons licence, unless indicated otherwise in a credit line to the material. If material is not included in the article's Creative Commons licence and your intended use is not permitted by statutory regulation or exceeds the permitted use, you will need to obtain permission directly from the copyright holder. To view a copy of this licence, visit http://creativecommons.org/licenses/by-nc-nd/4.0/.

© The Author(s) 2025